Deep Learning for Bayesian Optimization of Scientific Problems with High-Dimensional Structure

Anonymous authors
Paper under double-blind review

Abstract

Bayesian optimization (BO) is a popular paradigm for global optimization of expensive black-box functions, but there are many domains where the function is not completely a black-box. The data may have some known structure (e.g. symmetries) and/or the data generation process may be a composite process that yields useful intermediate or auxiliary information in addition to the value of the optimization objective. However, surrogate models traditionally employed in BO, such as Gaussian Processes (GPs), scale poorly with dataset size and do not easily accommodate known structure. Instead, we use Bayesian neural networks, a class of scalable and flexible surrogate models with inductive biases, to extend BO to complex, structured problems with high dimensionality. We demonstrate BO on a number of realistic problems in physics and chemistry, including topology optimization of photonic crystal materials using convolutional neural networks, and chemical property optimization of molecules using graph neural networks. On these complex tasks, we show that neural networks often outperform GPs as surrogate models for BO in terms of both sampling efficiency and computational cost.

1 Introduction

Bayesian optimization (BO) is a methodology well-suited for global (as opposed to local) optimization of expensive, black-box (e.g. derivative-free) functions and has been successfully applied to a wide range of problems in science and engineering (Ueno et al., 2016; Griffiths & Hernández-Lobato, 2020; Korovina et al., 2020) as well as hyperparameter tuning of machine learning models (Snoek et al., 2012; Swersky et al., 2014; Klein et al., 2017; Turner et al., 2020; Ru et al., 2021). BO works by iteratively deciding the next data point to label in order to maximize sampling efficiency and minimize the number of data points required to optimize a function, which is critical in many contexts where experiments or simulations can be costly or time-consuming.

However, in many domains, the system is not a complete black box. For example, complex, high-dimensional input spaces such as images or molecules have some known structure, symmetries and invariances. In addition, the function may be decomposed into other functions; rather than directly outputting the value of the objective, the data collection process may provide intermediate or auxiliary information from which the objective function can be cheaply computed. For example, a scientific experiment or simulation may produce a high-dimensional observation or multiple measurements simultaneously, such as the optical scattering spectrum of a nanoparticle over a range of wavelengths, or multiple quantum chemistry properties of a molecule from a single density functional theory (DFT) calculation. All of these physically-informed insights into the system are potentially useful and important factors for designing surrogate models through inductive biases, but they are often not fully exploited in existing methods and applications.

BO relies on specifying a surrogate model which captures a distribution over potential functions to incorporate uncertainty in its predictions. These surrogate models are typically Gaussian Processes (GPs), as the posterior distribution of GPs can be expressed analytically. However, (1) inference in GPs scales in time with the number of observations and output dimensionality, limiting their use to smaller datasets or to problems with low output dimensionality without the use of kernel approximations, and (2) GPs operate most

naturally over continuous low-dimensional input spaces, so kernels for high-dimensional data with complex structure must be carefully formulated and tuned by hand for each new domain. Thus, encoding inductive biases can be challenging.

Neural networks (NNs) and Bayesian neural networks (BNNs) have been proposed as an alternative to GPs due to their scalability and flexibility (Snoek et al., 2015; Springenberg et al., 2016). Alternatively, neural networks have also been used to create continuous latent spaces so that BO with vanilla GPs can be more easily applied (Kusner et al., 2017; Tripp et al., 2020). The ability to incorporate a variety of constraints, symmetries, and inductive biases into BNN architectures offers the potential for BO to be applied to more complex tasks with structured data.

This work demonstrates the use of deep learning to enable BO for complex, real-world scientific datasets, without the need for pre-trained models. In particular:

- We take advantage of auxiliary or intermediate information to improve BO for tasks with high-dimensional observations.
- We demonstrate BO on complex input spaces including images and molecules using convolutional and graph neural networks, respectively.
- We apply BO to several realistic scientific datasets, including the optical scattering of a nanoparticle, topology optimization of a photonic crystal material, and chemical property optimization of molecules from the QM9 dataset.

We show that neural networks are often able to significantly outperform GPs as surrogate models on these problems, and we believe that these strong results will also generalize to other contexts and enable BO to be applied to a wider range of problems. We note that while our methods are based on existing methods, we use a novel combination of these methods to tailor existing BO frameworks to real-world, complex applications.

1.1 Related Work

Various methods have been formulated to scale GPs to larger problems. For example, Ref Bruinsma et al. (2020) proposes a framework for multi-output GPs that scale linearly with m, where m is the dimensionality of a low-dimensional sub-space of the data. Ref Maddox et al. (2021a) uses multi-task GPs to perform BO over problems with large output dimensionalities. Additionally, GPs have been demonstrated on extremely large datasets through the use of GPUs and intelligent preconditioners Gardner et al. (2018); Wang et al. (2019) or through the use of various approximations Rahimi & Recht (2007); Wang et al. (2018); Liu et al. (2020); Maddox et al. (2021b).

GPs have been extended to complex problem settings to enable BO on a wider variety of problems. Astudillo & Frazier (2019) decompose synthetic problems as a composition of other functions, and take advantage of the additional structure to improve BO. However, the multi-output GP they use scales poorly with output dimensionality, and so this approach is limited to simpler problems. This work has also been extended Balandat et al. (2020); Maddox et al. (2021a). GP kernels have also been formulated for complex input spaces including convolutional kernels (Van der Wilk et al., 2017; Novak et al., 2020; Wilson et al., 2016) and graph kernels (Shervashidze et al., 2011; Walker & Glocker, 2019). The graph kernels have been used to apply BO to neural architecture search (NAS) where the architecture and connectivity of a neural network itself can be optimized (Ru et al., 2021).

Deep learning has been used as a scalable and flexible surrogate model for BO. In particular, ref. (Snoek et al., 2015) uses neural networks as an adaptive basis function for Bayesian linear regression, which allows BO to scale to large datasets. This approach also enables BO in more complex settings including transfer learning of the adaptive basis across multiple tasks, and modeling of auxiliary signals to improve performance (Perrone et al., 2018). Additionally, Bayesian neural networks (BNNs) that use Hamiltonian Monte Carlo to sample the posterior have been used for single-task and multi-task BO for hyperparameter optimization (Springenberg et al., 2016).

Another popular approach for BO on high-dimensional spaces is latent-space approaches. Here, an autoencoder such as a VAE is trained on a dataset to create a continuous latent space that represents the data. From here, a more conventional optimization algorithm, such as BO using GPs, can be used to optimize over the continuous latent space. This approach has been applied to complex tasks such as arithmetic expression optimization and chemical design (Kusner et al., 2017; Gómez-Bombarelli et al., 2018; Griffiths & Hernández-Lobato, 2020; Tripp et al., 2020; Deshwal & Doppa, 2021). Note that these approaches focus on both data generation and optimization simultaneously, whereas our work focuses on just the optimization process.

Random forests have also been used for iterative optimization such as sequential model-based algorithm configuration (SMAC) as they do not face scaling challenges (Hutter et al., 2011). Tree-structured Parzen Estimators (TPE) are also a popular choice for hyper-parameter tuning (Bergstra et al., 2013). However, these approaches still face the same issues with encoding complex, structured inputs such as images and graphs .

Deep learning has also been applied to improve tasks other than BO. For example, active learning is a similar scheme to BO that, instead of optimizing an objective function, aims to optimize the predictive ability of a model with as few data points as possible. The inductive biases of neural networks has enabled active learning on a variety of high-dimensional data including images (Gal et al., 2017), language (Siddhant & Lipton, 2018), and partial differential equations (Zhang et al., 2019a). BNNs have also been applied to the contextual bandits problem, where the model chooses between discrete actions to maximize expected reward (Blundell et al., 2015; Riquelme et al., 2018).

2 Bayesian Optimization

Now, we briefly introduce the BO methodology; more details can be found in the literature (Brochu et al., 2010; Shahriari et al., 2015; Garnett, 2022). We formulate our optimization task as a maximization problem in which we wish to find the input $\mathbf{x}^* \in \mathcal{X}$ that maximizes some function f such that $\mathbf{x}^* = \arg\max_{\mathbf{x}} f(\mathbf{x})$. The input x is most simply a real-valued vector, but can be generalized to categorical variables, images, or even discrete objects such as molecules. The function f returns the value of the objective $y = f(x)$ (which we also refer to as the "label" of x), and can represent some performance metric that we wish to maximize. Additionally, in general f can be a noisy function.

A key ingredient in BO is the surrogate model that produces a distribution of predictions as opposed to a single point estimate for the prediction. Such surrogate models are ideally Bayesian models, but in practice, a variety of approximate Bayesian models or even frequentist (i.e. empirical) distributions have been used. In iteration N, a Bayesian surrogate model $\mathcal{M}$ is trained on a labeled dataset $\mathcal{D}_{\text{train}} = \{(\mathbf{x}_n, y_n)\}_{n=1}^N$. An acquisition function α then uses $\mathcal{M}$ to suggest the next data point $\mathbf{x}_{N+1} \in \mathcal{X}$ to label, where

$$\mathbf{x}_{N+1} = \arg\max_{\mathbf{x}\in\mathcal{X}} \alpha\left(\mathbf{x}; \mathcal{M}, \mathcal{D}_{\text{train}}\right). \tag{1}$$

The new data is evaluated to get $y_{N+1} = f(\mathbf{x}_{N+1})$, and $(\mathbf{x}_{N+1}, y_{N+1})$ is added to $\mathcal{D}_{\text{train}}$.

2.1 Acquisition Function

An important consideration within BO is how to choose the next data point $\mathbf{x}_{N+1} \in \mathcal{X}$ given the model $\mathcal{M}$ and labelled dataset $\mathcal{D}_{\text{train}}$. This is parameterized through the "acquisition function" α, which we maximize to get the next data point to label as shown in Equation 1.

We choose the expected improvement (EI) acquisition function α_{EI} (Jones et al., 1998). When the posterior predictive distribution of the surrogate model $\mathcal{M}$ is a normal distribution $\mathcal{N}(\mu(\mathbf{x}), \sigma^2(\mathbf{x}))$, EI can be expressed analytically as

$$\alpha_{\text{EI}}(\mathbf{x}) = \sigma(\mathbf{x})\left[\gamma(\mathbf{x})\Phi(\gamma(\mathbf{x})) + \phi(\gamma(\mathbf{x}))\right], \tag{2}$$

where $\gamma(\mathbf{x}) = (\mu(\mathbf{x}) - y_{\text{best}})/\sigma(\mathbf{x})$, $y_{\text{best}} = \max(\{y_n\}_{n=1}^N)$ is the best value of the objective function so far, and ϕ and Φ are the PDF and CDF of the standard normal $\mathcal{N}(0, 1)$, respectively. For surrogate models that

do not give an analytical form for the posterior predictive distribution, we sample from the posterior N_{MC} times and use a Monte Carlo approximation of EI:

$$\alpha_{\text{EI-MC}}(\mathbf{x}) = \frac{1}{N_{\text{MC}}} \sum_{i=1}^{N_{\text{MC}}} \max\left(\mu^{(i)}(\mathbf{x}) - y_{\text{best}}, 0\right). \tag{3}$$

where $\mu^{(i)}$ is a prediction sampled from the posterior of $\mathcal{M}$ (Wilson et al., 2018).

2.2 Continued Training with Learning Rate Annealing

One challenge is that training a surrogate model on $\mathcal{D}_{\text{train}}$ from scratch in every optimization loop adds a large computational cost that limits the applicability of BO, especially since neural networks are ideally trained for a long time until convergence. To minimize the training time of BNNs in each optimization loop, we use the model that has been trained in the Nth optimization loop iteration as the initialization (also known as a "warm start") for the $(N+1)$th iteration, rather than training from a random initialization. In particular, we use the cosine annealing learning rate proposed in Loshchilov & Hutter (2016) which starts with a large learning rate and drops the learning rate to 0. For more details, refer to Section A.3 in the Appendix.

2.3 Auxiliary Information

Typically we assume f is a black box function, so we train $\mathcal{M}\colon \mathcal{X} \to \mathcal{Y}$ to model f. Here we consider the case where the experiment or observation may provide some intermediate or auxiliary information $\mathbf{z} \in \mathcal{Z}$, such that f can be decomposed as

$$f(\mathbf{x}) = h(g(\mathbf{x})), \tag{4}$$

where $g\colon \mathcal{X} \to \mathcal{Z}$ is the expensive labeling process, and $h\colon \mathcal{Z} \to \mathcal{Y}$ is a known objective function that can be cheaply computed. Note that this is also known as "composite functions" (Astudillo & Frazier, 2019; Balandat et al., 2020). In this case, we train $\mathcal{M}\colon \mathcal{X} \to \mathcal{Z}$ to model g, and the approximate EI acquisition function becomes

$$\alpha_{\text{EI-MC-aux}}(\mathbf{x}) = \frac{1}{N_{\text{MC}}} \sum_{i=1}^{N_{\text{MC}}} \max\left(h\left(\mu^{(i)}(\mathbf{x})\right) - y_{\text{best}}, 0\right). \tag{5}$$

which can be seen as a Monte Carlo version of the acquisition function presented in Astudillo & Frazier (2019). We denote models trained using auxiliary information with the suffix "-aux."

3 Surrogate Models

Bayesian models are able to capture uncertainty associated with both the data and the model parameters in the form of probability distributions. To do this, there is a *prior* probability distribution $P(\theta)$ placed upon the model parameters, and the *posterior* belief of the model parameters can be calculated using Bayes' theorem upon observing new data. Fully Bayesian neural networks have been studied in small architectures, but are impractical for realistically-sized neural networks as the nonlinearities between layers render the posterior intractable, thus requiring the use of MCMC methods to sample the posterior. In the last decade, however, there have been numerous proposals for approximate Bayesian neural networks that are able to capture some of the Bayesian properties and produce a predictive probability distribution. In this work, we compare several different options for the BNN surrogate model. In addition, we compare against other non-BNN baselines.

Ensembles combine multiple models into one model to improve predictive performance by averaging the results of the single models, and have been reported to be more robust than other BNNs (Ovadia et al., 2019). We build an ensemble of neural networks with identical architectures but different random initializations, which provide enough variation for the individual models to give different predictions. The different predictions of an ensemble can be interpreted as sampling from a posterior distribution, and so we use Eq. 5 for acquisition. Our ensemble size is $N_{\text{MC}} = 10$.

Variational BNNs model a prior and posterior distribution over the neural network weights, but use some approximation on the distributions to make the BNN tractable. In particular, we use Bayes by Backprop (BBB) (also referred to as the "mean field" approximation), which approximates the posterior over the neural network weights with independent normal distributions (Blundell et al., 2015). We also compare Multiplicative Normalizing Flows (MNF), which uses normalizing flows on top of each layer output for more expressive posterior distributions (Louizos & Welling, 2017).

BOHAMIANN proposed to use BNNs in BO by using stochastic gradient Hamiltonian Monte Carlo (SGHMC) to approximately sample the BNN posterior, combined with scale adaptation to adapt it for an iterative setting (Springenberg et al., 2016).

Neural Linear trains a conventional neural network on the data, but then replaces the last layer with Bayesian linear regression such that the neural network serves as an adaptive basis for the linear regression (Snoek et al., 2015).

GP Baselines. GPs are largely defined by their kernel (also called "covariance functions") which determines the prior and posterior distribution, how different data points relate to each other, and the type of data the GP can operate on. In this work, we will use **GP** to refer to a specific, standard specification that uses a Matérn 5/2 kernel, a popular kernel that operates over real-valued continuous spaces. To operate on images, we use a convolutional kernel, labeled as **ConvGP**, which is implemented using the infinite-width limit or infinite-ensemble limit of a convolutional neural network (Novak et al., 2020). Finally, to operate directly on graphs, we use the Weisfeiler-Lehman (WL) kernel as implemented by (Ru et al., 2021). They proposed to use the WL kernel to optimize neural network architectures in a method they call NAS-BOWL. Additionally, we compare against **GP-aux** which use multi-output GPs for problems with auxiliary information (also known as composite functions) (Astudillo & Frazier, 2019). In the Appendix, we also look at GPs that use infinite-width and infinite-ensemble neural network limits as the kernel (Novak et al., 2020).

VAE-GP uses a VAE trained on an unlabelled dataset to produce a continuous latent space over which conventional GP-based BO can be applied. In particular, we modified the implementation provided by (Tripp et al., 2020) in which they use a junction tree VAE (JTVAE) to encode chemical molecules (Jin et al., 2018). More details can be found in the Appendix.

Other Baselines. We compare against several global optimization algorithms that do not use Bayesian surrogate models and are cheap to run. **LIPO** is a parameter-free algorithm that assumes the underlying function is a Lipschitz function and estimates the bounds of the function (Malherbe & Vayatis, 2017; King, 2009). **DIRECT-L** (DIviding RECTangles-Local) systematically divides the search domain into smaller and smaller hyperrectangles to efficiently search the space (Gablonsky & Kelley, 2001; Johnson, 2010). **CMA-ES** (covariance matrix adaptation evolution strategy) is an evolutionary algorithm that samples new data based on a multivariate normal distribution and refines the parameters of this distribution until reaching convergence.

We emphasize that ensembles and variational methods can easily scale up to high-dimensional outputs with minimal increase in computational cost by simply changing the output layer size. Neural Linear and GPs scale cubically with output dimensionality (without the use of covariance approximations), making them difficult to train on high-dimensional auxiliary or intermediate information.

4 Results

We now look at three real-world scientific optimization tasks all of which provide intermediate or auxiliary information that can be leveraged. In the latter two tasks, the structure of the data also becomes important and hence BNNs with various inductive biases significantly outperform GPs and other baselines. For simplicity, we only highlight results from select architectures (see Appendix for full results along with dataset and hyperparameter details). All BO results are averaged over multiple trials, and the shaded area in the plots represents $\pm$ one standard error over the trials.

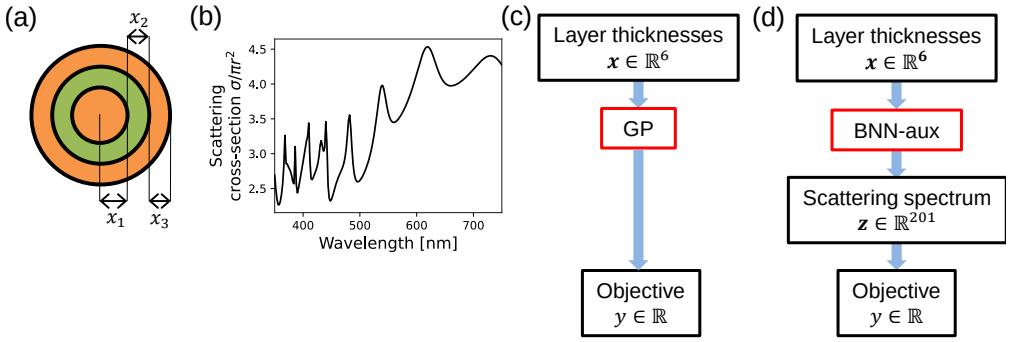

Figure 1: (a) A cross-section of a three-layer nanoparticle parameterized by the layer thicknesses. (b) An example of the scattering cross-section spectrum of a six-layer nanoparticle. (c) Whereas GPs are trained to directly predict the objective function, (d) multi-output BNNs can be trained with auxiliary information, which here is the scattering spectrum.

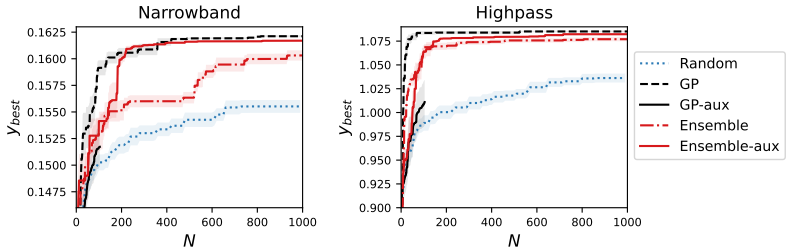

Figure 2: BO results for two different objective functions for the nanoparticle scattering problem. Training with auxiliary information (where $\mathcal{M}$ is trained to predict $\mathbf{z}$) is denoted with "-aux". Adding auxiliary information to BNNs significantly improves performance.

4.1 Multilayer Nanoparticle

We first consider the simple problem of light scattering from a multilayer nanoparticle, which has a wide variety of applications that demand a tailored optical response (Ghosh Chaudhuri & Paria, 2012) including biological imaging (Saltsberger et al., 2012), improved solar cell efficiency (Ho et al., 2012; Shi et al., 2013), and catalytic materials (Tang & Henkelman, 2009). In particular, the nanoparticle we consider consists of a lossless silica core and 5 spherical shells of alternating TiO_2 and silica. The nanoparticle is parameterized by the core radius and layer thicknesses as shown in Figure 1(a), which we restrict to the range 30 nm to 70 nm. Because the size of the nanoparticle is on the order of the wavelength of light, its optical properties can be tuned by the number and thicknesses of the layers. The scattering spectrum can be calculated semi-analytically, as detailed in Section A.1.1 of the Appendix.

We wish to optimize the scattering cross-section spectrum over a range of visible wavelengths, an example of which is shown in Figure 1(b). In particular, we compare two different objective functions: the narrowband objective that aims to maximize scattering in the small wavelength range 600 nm to 640 nm and minimize it elsewhere, and the highpass objective that aims to maximize scattering above 600 nm and minimize it elsewhere. While conventional GPs train using the objective function as the label directly, BNNs with auxiliary information can be trained to predict the full scattering spectrum, i.e. the auxiliary information $\mathbf{z} \in \mathbb{R}^{201}$, which is then used to calculate the objective function, as shown in Figure 1(c,d).

BO results are shown in Figure 2. Adding auxiliary information significantly improves BO performance for ensembles. Additionally, they are competitive with GPs, making BNNs a viable approach for scaling BO to large datasets. In the Appendix, we see similar trends for other types of BNNs. Due to poor scaling of multi-output GPs with respect to output dimensionality, we are only able to run GP-aux for a small number of iterations in a reasonable time. Within these few iterations, GP-aux performs poorly, only

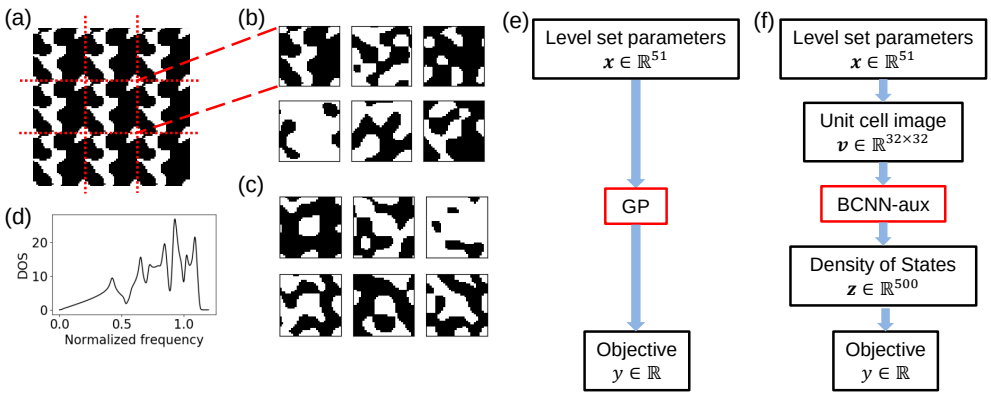

Figure 3: (a) A 2D photonic crystal (PC). The black and white regions represent different materials, and the periodic unit cells are outlined in red. Examples of PC unit cells drawn from the (b) PC-A distribution and (c) the PC-B distributions. The PC-A data distribution is translation invariant, whereas unit cells drawn from the PC-B distribution all have white regions in the middle of the unit cell, so the distribution is not translation invariant. (d) Example of a PC density of states (DOS). (e, f) Comparison of the process flow for training the surrogate model in the case of (e) GPs and (f) Bayesian Convolutional NNs (BCNN). The BCNN can train directly on the images to take advantage of the structure and symmetries in the data, and predict the multi-dimensional DOS.

slightly better than random sampling. We also see in the Appendix that BO with either GPs or BNNs are comparable with, or outperform other global optimization algorithms, including DIRECT-L and CMA-ES. Surprisingly, BO using an infinite ensemble of infinite-width networks performs poorly compared to normal ensembles, suggesting that the infinite-width formulations do not fully capture the dynamics of their finite-width counterparts.

4.2 Photonic Crystal Topology

Next we look at a more complex, high-dimensional domain that contains symmetries not easily exploitable by GPs. Photonic crystals (PCs) are nanostructured materials that are engineered to exhibit exotic optical properties not found in bulk materials, including photonic band gaps, negative index of refraction, and angular selective transparency (John, 1987; Yablonovitch, 1987; Joannopoulos et al., 2008; Shen et al., 2014). As advanced fabrication techniques are enabling smaller and smaller feature sizes, there has been growing interest in inverse design and topology optimization to design even more sophisticated PCs (Jensen & Sigmund, 2011; Men et al., 2014) for applications in photonic integrated circuits, flat lenses, and sensors (Piggott et al., 2015; Lin et al., 2019).

Here we consider 2D PCs consisting of periodic unit cells represented by a 32×32 pixel image, as shown in Figure 3(a), with white and black regions representing vacuum (or air) and silicon, respectively. Because optimizing over raw pixel values may lead to pixel-sized features or intermediate pixel values that cannot be fabricated, we have parameterized the PCs with a level-set function $\phi\colon \mathcal{X} \to \mathcal{V}$ that converts a 51-dimensional feature vector $\mathbf{x} = [c_1, c_2, ..., c_{50}, \Delta] \in \mathbb{R}^{51}$ representing the level-set parameters into an image $\mathbf{v} \in \mathbb{R}^{32\times32}$ that represents the PC. More details can be found in Section A.1.2 in the Appendix.

We test BO on two different data distributions, which are shown in Figure 3(b,c). In the PC-A distribution, $\mathbf{x}$ spans $c_i \in [-1, 1]\,, \Delta \in [-3, 3]$. In the PC-B distribution, we arbitrarily restrict the domain to $c_i \in [0, 1]$. The PC-A data distribution is translation invariant, meaning that any PC with a translational shift will also be in the data distribution. However, the PC-B data distribution is not translation invariant, as shown by the white regions in the center of all the examples in Figure 3(c).

The optical properties of PCs can be characterized by their photonic density of states (DOS), e.g. see Figure 3(d). We choose an objective function that aims to minimize the DOS in a certain frequency range while

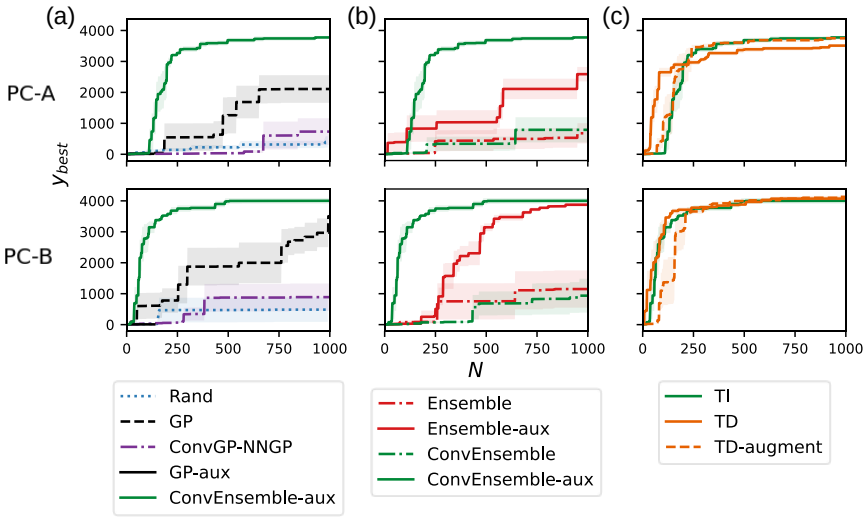

Figure 4: Three sets of comparisons for BO results on the (top row) PC-A and (bottom row) PC-B datasets. (a) BNNs with inductive biases outperform all other GP baselines and the random baseline. Note that GP-aux is comparable to random sampling. (b) The inductive bias of convolutional layers and the addition of auxiliary information significantly improve performance of BCNNs. (c) Data augmentation boosts performance if the augmentations reflect a symmetry present in the dataset but not enforced by the model architecture. "TI" refers to a translation invariant BCNN architecture, whereas "TD" refers to a translation dependent architecture. "-augment" signifies that data augmentation of the photonic crystal image is applied, which includes periodic translations, flips, and rotations.

maximizing it everywhere else, which corresponds to opening up a photonic band gap in said frequency range. As shown in Figure 3(e,f), we train GPs directly on the level-set parameters $\mathcal{X}$, whereas we train the Bayesian convolutional NNs (BCNNs) on the more natural unit cell image space $\mathcal{V}$. BCNNs can also be trained to predict the full DOS as auxiliary information $\mathbf{z} \in \mathbb{R}^{500}$.

The BO results, seen in Figure 4(a), show that BCNNs outperform GPs by a significant margin on both datasets, which is due to both the auxiliary information and the inductive bias of the convolutional layers, as shown in Figure 4(b). Because the behavior of PCs is determined by their topology rather than individual pixel values or level-set parameters, BCNNs are much better suited to analyze this dataset compared to GPs. Additionally, BCNNs can be made much more data-efficient since they directly encode translation invariance and thus learn the behavior of a whole class of translated images from a single image. Because GP-aux is extremely expensive compared to GP (500× longer on this dataset), we are only able to run GP-aux for a small number of iterations, where it performs comparably to random sampling. We also compare to GPs using a convolutional kernel ("ConvGP-NNGP") in Figure 4(a). ConvGP-NNGP only performs slightly better than random sampling, which is likely due to a lack of auxiliary information and inflexibility to learn the most suitable representation for this dataset.

For our main experiments with BCNNs, we use an architecture that respects translation invariance. To demonstrate the effect of another commonly used deep learning training technique, we also experiment with incorporating translation invariance into a translation dependent (i.e. *not* translation invariant) architecture using a data augmentation scheme in which each image is randomly translated, flipped, and rotated during training. We expect data augmentation to improve performance when the data distribution exhibits the corresponding symmetries: in this case, we focus on translation invariance. As shown in Figure 4(c), we indeed find that data augmentation improves the BO performance of the translation dependent architecture when trained on the translation invariant PC-A dataset, even matching the performance of a translation invariant architecture on PC-A. However, on the translation dependent PC-B dataset, data augmentation initially hurts the BO performance of the translation dependent architecture because the model is unable to quickly specialize to the more compact distribution of PC-B, putting its BO performance more on par with

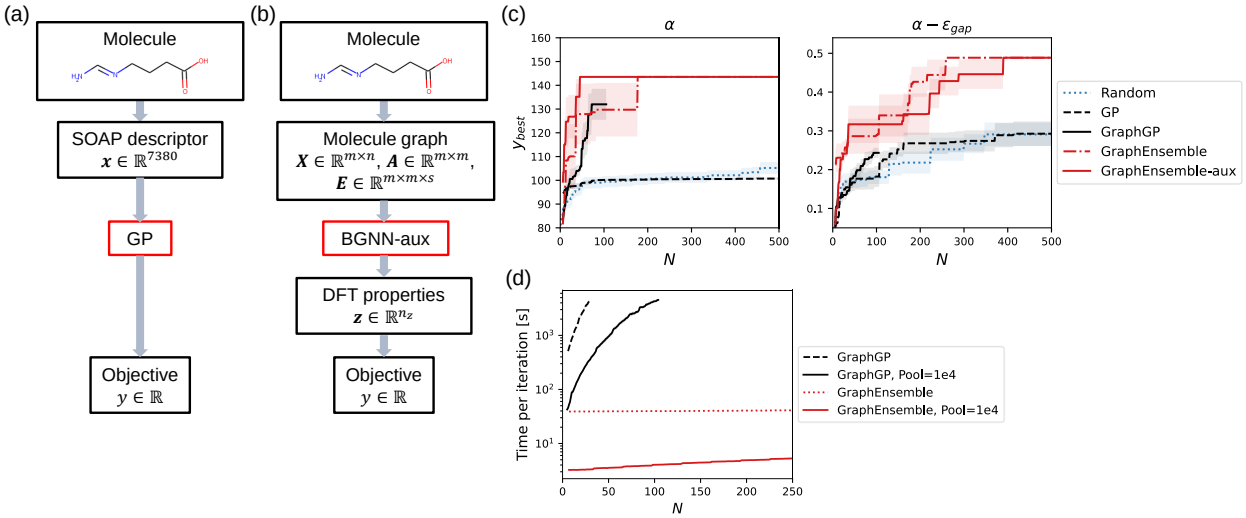

Figure 5: Quantum chemistry task and results. (a) The GP is trained on the SOAP descriptor, which is precomputed for each molecule. (b) The BGNN operates directly on a graph representation of the molecule, where atoms and bonds are represented by nodes and edges, respectively. The BGNN can be trained on multiple properties given in the QM9 dataset. (c) BO results for various properties. (d) Time per BO iteration. (Note the logarithmic scale on the y-axis.) GraphGP takes orders of magnitudes longer than BGNNs for moderate N.

models trained on PC-A. These results show that techniques used to improve generalization performance (such as data augmentation or invariant architectures) for training deep learning architectures can also be applied to BO surrogate models and, when used appropriately, directly translate into improved BO performance. Note that data augmentation would not be feasible for GPs without a hand-crafted kernel as the increased size of the dataset would cause inference to become computationally intractable.

4.3 Organic Molecule Quantum Chemistry

Finally, we optimize the chemical properties of molecules. Chemical optimization is of huge interest with applications in drug design and materials optimization (Hughes et al., 2011). This is a difficult problem where computational approaches such as density functional theory (DFT) can take days for simple molecules and are intractable for larger molecules; synthesis is expensive and time-consuming, and the space of synthesizable molecules is large and complex. There have been many approaches for molecular optimization that largely revolve around finding a continuous latent space of molecules (Gómez-Bombarelli et al., 2018) or hand-crafting kernels (Korovina et al., 2020).

Here we focus on the QM9 dataset (Ruddigkeit et al., 2012; Ramakrishnan et al., 2014), which consists of 133,885 small organic molecules along with their geometric, electronic, and thermodynamics quantities that have been calculated with DFT. Instead of optimizing over a continuous space, we draw from the fixed pool of available molecules and iteratively select the next molecule to add to $\mathcal{D}_{\text{train}}$. This is a problem setting especially common to materials design where databases are incomplete and the space of experimentally-known materials is small.

Here we use a Bayesian graph neural network (BGNN) for our surrogate model, as GNNs have become popular for chemistry applications due to the natural encoding of a molecule as a graph with atoms and bonds as nodes and edges, respectively. For the GP baseline, we use the Smooth Overlap of Atomic Positions (SOAP) descriptor to produce a fixed-length feature vector for each molecule, as shown in Figure 5(a) (De et al., 2016; Himanen et al., 2020).

We compare two different optimization objectives derived from the QM9 dataset: the isotropic polarizability α and $(\alpha - \epsilon_{\text{gap}})$ where ϵ_{gap} is the HOMO-LUMO energy gap. Because many of the chemical properties in the QM9 dataset can be collectively computed by a single DFT or molecular dynamics calculation, we can treat a group of labels from QM9 as auxiliary information $\mathbf{z}$ and train our BGNN to predict this entire group simultaneously. The objective function h then simply picks out the property of interest.

As shown in Figure 5(c), BGNNs and GraphGPs significantly outperform GPs, showing that the inductive bias in the graph structure leads to a much more natural representation of the molecule and its properties. In the case of maximizing the polarizability α, including the auxiliary information improves BO performance, showing signs of positive transfer. As seen in Figure 5(d), we also note that the GraphGP is relatively computationally expensive (15× longer than GPs for small N and 800× longer than BGNNs for $N = 100$) and so we are only able to run it for a limited N in a reasonable time frame. We see that BGNNs perform comparably or better than GraphGPs despite incurring a fraction of the computational cost.

5 Discussion

Introducing physics-informed priors (in the form of inductive biases) into the model are critical for their performance. Well-known inductive biases in deep learning include convolutional and graph neural networks for images and graph structures (e.g. chemical molecules), which we see significantly improve BO performance. Another inductive bias that we introduce is the addition of auxiliary information present in composite functions, which significantly improves the performance of BO for the nanoparticle and photonic crystal tasks. We conjecture that the additional information forces the BNN to learn a more consistent physical model of the system since it must learn features that are shared across the multi-dimensional auxiliary information, thus enabling the BNN to generalize better. For example, the scattering spectrum of the multilayer particle consists of multiple resonances (sharp peaks), the width and location of which are determined by the material properties and layer thicknesses. The BNN could potentially learn these more abstract features, and thus, the deeper physics, to help it interpolate more efficiently (Peurifoy et al., 2018). It is also possible that the loss landscape for the auxiliary information is smoother than that of the objective function and that the auxiliary information acts as an implicit regularization that improves generalization performance.

For the quantum chemistry task, using auxiliary information improves performance for one of the two properties we optimized. This is likely due to the small size of the available auxiliary information (only a handful of chemical properties from the QM dataset) as compared with the other two tasks. In a more realistic online setting, we would have significantly more physically-informative information available from a DFT calculation, e.g. we could easily compute the electronic density of states (the electronic analogue of the auxiliary information used in the photonics task).

Interestingly, GP-aux performs extremely poorly on the nanoparticle and photonic crystal tasks. One possible reason is that we are only able to run GP-aux for a few iterations, and it is not uncommon for GP-based BO to require some critical number of iterations to reach convergence especially in the case of high-dimensional systems where the size of the covariance matrix scales with the square of the dimensionality. It may also be possible that GP-aux only works on certain types of decompositions of functions and cannot be applied broadly to all composite functions, as the inductive biases in GPs are often hard-coded.

There is an interesting connection between how well BNNs are able to capture and explore a multi-modal posterior distribution and their performance in BO. For example, we have noticed that larger batch sizes tend to significantly hurt BO performance. On the one hand, larger batch sizes may be resulting in poorer generalization as the model finds sharper local minima in the loss landscape. Another explanation is that the stochasticity inherent in smaller batch sizes allows the BNN to more easily explore the posterior distribution, which is known to be highly multi-modal (Fort et al., 2019). Indeed, BO often underperforms for very small dataset sizes N but quickly catches up as N increases, indicating that batch size is an important hyperparameter which must be balanced with computational cost.

All our results use continued training (or warm restart) to minimize training costs. We note that re-initializing $\mathcal{M}$ and training from scratch in every iteration performs better than continued training on some tasks (results in the Appendix), which points to how BNNs may not sufficiently represent a multi-modal posterior

distribution or that continued training may skew the training distribution that the BNN sees. Future work will consider using stochastic training approaches such as SG-MCMC methods for exploring posterior distributions (Welling & Teh, 2011; Zhang et al., 2019b) as well as other continual learning techniques to further minimize training costs, especially for larger datasets (Parisi et al., 2019).

When comparing BNN architectures, we find that ensembles tend to consistently perform among the best, which is supported by previous literature showing that ensembles capture uncertainty much better than variational methods (Ovadia et al., 2019; Gustafsson et al., 2020) especially in multi-modal loss landscapes (Fort et al., 2019). Ensembles are also attractive because they require no additional hyperparameters and they are simple to implement. Although training costs increase linearly with the size of the ensemble, this can be easily parallelized on modern computing infrastructures. Furthermore, recent work that aims to model efficient ensembles that minimize computational cost could be an interesting future direction (Havasi et al., 2020; Wen et al., 2020).

BBB performs reasonably well and is competitive with or even better than ensembles on some tasks, but it requires significant hyperparameter tuning. The tendency of variational methods such as BBB to underestimate uncertainty is likely detrimental to their performance in BO. Additionally, Sun et al. (2019) shows that BBB has trouble scaling to larger network sizes, which may make them unsuitable for more complex tasks such as those in our work. Neural Linear methods are quite powerful and cheap, making them very promising for tasks without high-dimensional auxiliary information. Integrating Neural Linear with multi-output GPs is an interesting direction for future work. BOHAMIANN performs very well on the nanoparticle narrow-band objective and comparable to other BNNs without auxiliary information on the nanoparticle highpass objective. This is likely due to its effectiveness in exploring a multi-modal posterior. However, the need for SGHMC to sample the posterior makes this method computationally expensive, and so we were only able to run it for a limited number of iterations using a small neural network architecture.

Infinitely wide neural networks are another interesting research direction, as the ability to derive infinitely wide versions of various neural network architectures such as convolutions, and more recently graph convolutional layers (Hu et al., 2020) could potentially bring the power of GPs and BO to complex problems in low-data regimes. However, we find they perform relatively poorly in BO, are quite sensitive to hyperparameters (e.g. kernel and parameterization), and current implementations of certain operations such as pooling are too slow for practical use in an iterative setting.

As seen in Appendix A.8, VAE-GP performs worse than our method on two of the chemistry objectives and better on one objective. While latent-space optimization methods are often applied to domains where one wants to simultaneously generate data and optimize over the data distribution, these methods can also be applied to the cases in this work, where a data pool (e.g. QM9 dataset for the chemistry task) or separate data generation process (e.g. level-set process for the photonic crystal task) is already available. In these cases, the VAE is not used as a generative model, but rather as a way to learn appropriate representations. While latent-space approaches are able to take advantage of well-developed and widely available optimization algorithms, they also require unsupervised pre-training on a sizeable dataset and a suitable autoencoder model with the necessary inductive biases. Such models are available in chemistry where there have been significant development, but are more limited in other domains such as photonics. On the other hand, our method is able to incorporate the data structure or domain knowledge in an end-to-end manner during training, although future work is needed to more carefully evaluate how much of an advantage this is and whether it depends on specific dataset or domain characteristics. For settings where we do not need a generative model, it would also be interesting to replace the autoencoder with a self-supervised model (Hendrycks et al., 2019; Loh et al., 2021) or semi-supervised model (Kingma et al., 2014) to create a suitable latent space.

Non-Bayesian global optimization methods such as LIPO and DIRECT-L are quite powerful in spite of their small computational overhead and can even outperform BO on some simpler tasks. However, they are not as consistent as BO, performing more comparably to random sampling on other tasks. CMA-ES performs poorly on all the tasks here. Also, like GPs, these non-Bayesian algorithms assume a continuous input space and cannot be effectively applied to structured, high-dimensional problems.

6 Conclusion

We have demonstrated global optimization on multiple tasks using a combination of deep learning and BO. In particular, we have shown how BNNs can be used as surrogate models in BO, which enables the scaling of BO to large datasets and provides the flexibility to incorporate a wide variety of constraints, data augmentation techniques, and inductive biases. We have demonstrated that integrating domain-knowledge on the structure and symmetries of the data into the surrogate model as well as exploiting intermediate or auxiliary information significantly improves BO performance, all of which can be interpreted as physics-informed priors. Intuitively, providing the BNN surrogate model with all available information allows the BNN to learn a more faithful physical model of the system of interest, thus enhancing the performance of BO. Finally, we have applied BO to real-world, high-dimensional scientific datasets, and our results show that BNNs can outperform our best-effort GPs, even with strong domain-dependent structure encoded in the covariance functions. We note that our method is not necessarily tied to any particular application domain, and can lower the barrier of entry for design and optimization.

Future work will investigate more complex BNN architectures with stronger inductive biases. For example, output constraints can be placed through unsupervised learning (Karpatne et al., 2017) or by variationally fitting a BNN prior (Yang et al., 2020). Custom architectures have also been proposed for partial differential equations (Raissi et al., 2017; Lu et al., 2020), many-body systems (Cranmer et al., 2020), and generalized symmetries (Hutchinson et al., 2020), which will enable effective BO on a wider range of tasks. The methods and experiments presented here enable BO to be effectively applied in a wider variety of settings.

We make our datasets and code publicly available at `http://github.com/placeholder/deepBO`.

References

Raul Astudillo and Peter Frazier. Bayesian optimization of composite functions. In *International Conference on Machine Learning*, pp. 354–363. PMLR, 2019.

Maximilian Balandat, Brian Karrer, Daniel Jiang, Samuel Daulton, Ben Letham, Andrew G Wilson, and Eytan Bakshy. Botorch: a framework for efficient monte-carlo bayesian optimization. *Advances in neural information processing systems*, 33:21524–21538, 2020.

James Bergstra, Daniel Yamins, and David Cox. Making a science of model search: Hyperparameter optimization in hundreds of dimensions for vision architectures. In *International conference on machine learning*, pp. 115–123. PMLR, 2013.

Charles Blundell, Julien Cornebise, Koray Kavukcuoglu, and Daan Wierstra. Weight uncertainty in neural networks. *arXiv preprint arXiv:1505.05424*, 2015.

Eric Brochu, Vlad M Cora, and Nando De Freitas. A tutorial on bayesian optimization of expensive cost functions, with application to active user modeling and hierarchical reinforcement learning. *arXiv preprint arXiv:1012.2599*, 2010.

Wessel Bruinsma, Eric Perim, William Tebbutt, Scott Hosking, Arno Solin, and Richard Turner. Scalable exact inference in multi-output gaussian processes. In *International Conference on Machine Learning*, pp. 1190–1201. PMLR, 2020.

Miles Cranmer, Alvaro Sanchez-Gonzalez, Peter Battaglia, Rui Xu, Kyle Cranmer, David Spergel, and Shirley Ho. Discovering symbolic models from deep learning with inductive biases. *arXiv preprint arXiv:2006.11287*, 2020.

Sandip De, Albert P Bartók, Gábor Csányi, and Michele Ceriotti. Comparing molecules and solids across structural and alchemical space. *Physical Chemistry Chemical Physics*, 18(20):13754–13769, 2016.

Aryan Deshwal and Jana Doppa. Combining latent space and structured kernels for bayesian optimization over combinatorial spaces. *Advances in Neural Information Processing Systems*, 34, 2021.

Stanislav Fort, Huiyi Hu, and Balaji Lakshminarayanan. Deep ensembles: A loss landscape perspective. *arXiv preprint arXiv:1912.02757*, 2019.

Joerg M Gablonsky and Carl T Kelley. A locally-biased form of the direct algorithm. *Journal of Global Optimization*, 21(1):27–37, 2001.

Yarin Gal, Riashat Islam, and Zoubin Ghahramani. Deep bayesian active learning with image data. *arXiv preprint arXiv:1703.02910*, 2017.

Jacob Gardner, Geoff Pleiss, Kilian Q Weinberger, David Bindel, and Andrew G Wilson. Gpytorch: Blackbox matrix-matrix gaussian process inference with gpu acceleration. *Advances in neural information processing systems*, 31, 2018.

Roman Garnett. *Bayesian Optimization*. Cambridge University Press, 2022. in preparation.

Rajib Ghosh Chaudhuri and Santanu Paria. Core/shell nanoparticles: classes, properties, synthesis mechanisms, characterization, and applications. *Chemical reviews*, 112(4):2373–2433, 2012.

Rafael Gómez-Bombarelli, Jennifer N Wei, David Duvenaud, José Miguel Hernández-Lobato, Benjamín Sánchez-Lengeling, Dennis Sheberla, Jorge Aguilera-Iparraguirre, Timothy D Hirzel, Ryan P Adams, and Alán Aspuru-Guzik. Automatic chemical design using a data-driven continuous representation of molecules. *ACS central science*, 4(2):268–276, 2018.

Daniele Grattarola and Cesare Alippi. Graph neural networks in tensorflow and keras with spektral. *arXiv preprint arXiv:2006.12138*, 2020.

Ryan-Rhys Griffiths and José Miguel Hernández-Lobato. Constrained bayesian optimization for automatic chemical design using variational autoencoders. *Chemical science*, 11(2):577–586, 2020.

Fredrik K Gustafsson, Martin Danelljan, and Thomas B Schon. Evaluating scalable bayesian deep learning methods for robust computer vision. In *Proceedings of the IEEE/CVF Conference on Computer Vision and Pattern Recognition Workshops*, pp. 318–319, 2020.

Nikolaus Hansen, Youhei Akimoto, and Petr Baudis. CMA-ES/pycma on Github. Zenodo, DOI:10.5281/zenodo.2559634, February 2019. URL `https://doi.org/10.5281/zenodo.2559634`.

Marton Havasi, Rodolphe Jenatton, Stanislav Fort, Jeremiah Zhe Liu, Jasper Snoek, Balaji Lakshminarayanan, Andrew M Dai, and Dustin Tran. Training independent subnetworks for robust prediction. *arXiv preprint arXiv:2010.06610*, 2020.

Dan Hendrycks, Mantas Mazeika, Saurav Kadavath, and Dawn Song. Using self-supervised learning can improve model robustness and uncertainty. *Advances in neural information processing systems*, 32, 2019.

Lauri Himanen, Marc O. J. Jäger, Eiaki V. Morooka, Filippo Federici Canova, Yashasvi S. Ranawat, David Z. Gao, Patrick Rinke, and Adam S. Foster. DScribe: Library of descriptors for machine learning in materials science. *Computer Physics Communications*, 247:106949, 2020. ISSN 0010-4655. doi: 10.1016/j.cpc.2019.106949. URL `https://doi.org/10.1016/j.cpc.2019.106949`.

Chung-I Ho, Dan-Ju Yeh, Vin-Cent Su, Chieh-Hung Yang, Po-Chuan Yang, Ming-Yi Pu, Chieh-Hsiung Kuan, I-Chun Cheng, and Si-Chen Lee. Plasmonic multilayer nanoparticles enhanced photocurrent in thin film hydrogenated amorphous silicon solar cells. *Journal of Applied Physics*, 112(2):023113, 2012.

Jilin Hu, Jianbing Shen, Bin Yang, and Ling Shao. Infinitely wide graph convolutional networks: semi-supervised learning via gaussian processes. *arXiv preprint arXiv:2002.12168*, 2020.

Gao Huang, Yixuan Li, Geoff Pleiss, Zhuang Liu, John E Hopcroft, and Kilian Q Weinberger. Snapshot ensembles: Train 1, get m for free. *arXiv preprint arXiv:1704.00109*, 2017.

James P Hughes, Stephen Rees, S Barrett Kalindjian, and Karen L Philpott. Principles of early drug discovery. *British journal of pharmacology*, 162(6):1239–1249, 2011.

Michael Hutchinson, Charline Le Lan, Sheheryar Zaidi, Emilien Dupont, Yee Whye Teh, and Hyunjik Kim. Lietransformer: Equivariant self-attention for lie groups. *arXiv preprint arXiv:2012.10885*, 2020.

Frank Hutter, Holger H Hoos, and Kevin Leyton-Brown. Sequential model-based optimization for general algorithm configuration. In *International conference on learning and intelligent optimization*, pp. 507–523. Springer, 2011.

Jakob Søndergaard Jensen and Ole Sigmund. Topology optimization for nano-photonics. *Laser & Photonics Reviews*, 5(2):308–321, 2011.

Wengong Jin, Regina Barzilay, and Tommi Jaakkola. Junction tree variational autoencoder for molecular graph generation. In *International conference on machine learning*, pp. 2323–2332. PMLR, 2018.

John D. Joannopoulos, Steven G. Johnson, Joshua N. Winn, and Robert D. Meade. *Photonic Crystals: Molding the Flow of Light (Second Edition)*. Princeton University Press, 2 edition, 2008. ISBN 0691124566.

Sajeev John. Strong localization of photons in certain disordered dielectric superlattices. *Physical review letters*, 58(23):2486, 1987.

Steven G. Johnson. The nlopt nonlinear-optimization package, 2010. URL `http://github.com/stevengj/nlopt`.

Steven G Johnson and John D Joannopoulos. Block-iterative frequency-domain methods for maxwell's equations in a planewave basis. *Optics express*, 8(3):173–190, 2001.

Donald R. Jones, Matthias Schonlau, and William J. Welch. Efficient global optimization of expensive black-box functions. *Journal of Global Optimization*, 13(4):455–492, Dec 1998. ISSN 1573-2916. doi: 10.1023/A:1008306431147. URL `https://doi.org/10.1023/A:1008306431147`.

Anuj Karpatne, William Watkins, Jordan Read, and Vipin Kumar. Physics-guided neural networks (pgnn): An application in lake temperature modeling. *arXiv preprint arXiv:1710.11431*, 2017.

Davis E. King. Dlib-ml: A machine learning toolkit. *Journal of Machine Learning Research*, 10:1755–1758, 2009.

Durk P Kingma, Shakir Mohamed, Danilo Jimenez Rezende, and Max Welling. Semi-supervised learning with deep generative models. *Advances in neural information processing systems*, 27, 2014.

Aaron Klein, Stefan Falkner, Simon Bartels, Philipp Hennig, and Frank Hutter. Fast bayesian optimization of machine learning hyperparameters on large datasets. In *Artificial Intelligence and Statistics*, pp. 528–536. PMLR, 2017.

Ksenia Korovina, Sailun Xu, Kirthevasan Kandasamy, Willie Neiswanger, Barnabas Poczos, Jeff Schneider, and Eric Xing. Chembo: Bayesian optimization of small organic molecules with synthesizable recommendations. In *International Conference on Artificial Intelligence and Statistics*, pp. 3393–3403. PMLR, 2020.

Matt J Kusner, Brooks Paige, and José Miguel Hernández-Lobato. Grammar variational autoencoder. In *International conference on machine learning*, pp. 1945–1954. PMLR, 2017.

Zin Lin, Victor Liu, Raphaël Pestourie, and Steven G Johnson. Topology optimization of freeform large-area metasurfaces. *Optics express*, 27(11):15765–15775, 2019.

Boyuan Liu, Steven G Johnson, John D Joannopoulos, and Ling Lu. Generalized gilat–raubenheimer method for density-of-states calculation in photonic crystals. *Journal of Optics*, 20(4):044005, 2018.

Haitao Liu, Yew-Soon Ong, Xiaobo Shen, and Jianfei Cai. When gaussian process meets big data: A review of scalable gps. *IEEE transactions on neural networks and learning systems*, 31(11):4405–4423, 2020.

Charlotte Loh, Thomas Christensen, Rumen Dangovski, Samuel Kim, and Marin Soljacic. Surrogate- and invariance-boosted contrastive learning for data-scarce applications in science. *arXiv preprint arXiv:2110.08406*, 2021.

Ilya Loshchilov and Frank Hutter. Sgdr: Stochastic gradient descent with warm restarts. *arXiv preprint arXiv:1608.03983*, 2016.

Christos Louizos and Max Welling. Multiplicative normalizing flows for variational bayesian neural networks. *arXiv preprint arXiv:1703.01961*, 2017.

Peter Y Lu, Samuel Kim, and Marin Soljačić. Extracting interpretable physical parameters from spatiotemporal systems using unsupervised learning. *Physical Review X*, 10(3):031056, 2020.

Wesley J Maddox, Maximilian Balandat, Andrew G Wilson, and Eytan Bakshy. Bayesian optimization with high-dimensional outputs. *Advances in Neural Information Processing Systems*, 34, 2021a.

Wesley J Maddox, Samuel Stanton, and Andrew G Wilson. Conditioning sparse variational gaussian processes for online decision-making. *Advances in Neural Information Processing Systems*, 34, 2021b.

Cédric Malherbe and Nicolas Vayatis. Global optimization of lipschitz functions. *arXiv preprint arXiv:1703.02628*, 2017.

Han Men, Karen YK Lee, Robert M Freund, Jaime Peraire, and Steven G Johnson. Robust topology optimization of three-dimensional photonic-crystal band-gap structures. *Optics express*, 22(19):22632–22648, 2014.

Roman Novak, Lechao Xiao, Jiri Hron, Jaehoon Lee, Alexander A. Alemi, Jascha Sohl-Dickstein, and Samuel S. Schoenholz. Neural tangents: Fast and easy infinite neural networks in python. In *International Conference on Learning Representations*, 2020. URL `https://github.com/google/neural-tangents`.

Yaniv Ovadia, Emily Fertig, Jie Ren, Zachary Nado, David Sculley, Sebastian Nowozin, Joshua Dillon, Balaji Lakshminarayanan, and Jasper Snoek. Can you trust your model's uncertainty? evaluating predictive uncertainty under dataset shift. In *Advances in Neural Information Processing Systems*, pp. 13991–14002, 2019.

German I Parisi, Ronald Kemker, Jose L Part, Christopher Kanan, and Stefan Wermter. Continual lifelong learning with neural networks: A review. *Neural Networks*, 113:54–71, 2019.

Valerio Perrone, Rodolphe Jenatton, Matthias Seeger, and Cédric Archambeau. Scalable hyperparameter transfer learning. In *Proceedings of the 32nd International Conference on Neural Information Processing Systems*, pp. 6846–6856, 2018.

John Peurifoy, Yichen Shen, Li Jing, Yi Yang, Fidel Cano-Renteria, Brendan G DeLacy, John D Joannopoulos, Max Tegmark, and Marin Soljačić. Nanophotonic particle simulation and inverse design using artificial neural networks. *Science advances*, 4(6):eaar4206, 2018.

Alexander Y Piggott, Jesse Lu, Konstantinos G Lagoudakis, Jan Petykiewicz, Thomas M Babinec, and Jelena Vučković. Inverse design and demonstration of a compact and broadband on-chip wavelength demultiplexer. *Nature Photonics*, 9(6):374–377, 2015.

Wenjun Qiu, Brendan G DeLacy, Steven G Johnson, John D Joannopoulos, and Marin Soljačić. Optimization of broadband optical response of multilayer nanospheres. *Optics express*, 20(16):18494–18504, 2012.

Ali Rahimi and Benjamin Recht. Random features for large-scale kernel machines. *Advances in neural information processing systems*, 20, 2007.

Maziar Raissi, Paris Perdikaris, and George Em Karniadakis. Physics informed deep learning (part i): Data-driven solutions of nonlinear partial differential equations. *arXiv preprint arXiv:1711.10561*, 2017.

Raghunathan Ramakrishnan, Pavlo O Dral, Matthias Rupp, and O Anatole Von Lilienfeld. Quantum chemistry structures and properties of 134 kilo molecules. *Scientific data*, 1(1):1–7, 2014.

Carlos Riquelme, George Tucker, and Jasper Snoek. Deep bayesian bandits showdown: An empirical comparison of bayesian deep networks for thompson sampling. *arXiv preprint arXiv:1802.09127*, 2018.

Binxin Ru, Xingchen Wan, Xiaowen Dong, and Michael Osborne. Interpretable neural architecture search via bayesian optimisation with weisfeiler-lehman kernels. In *International Conference on Learning Representations*, 2021. URL `https://openreview.net/forum?id=j9Rv7qdXjd`.

Lars Ruddigkeit, Ruud Van Deursen, Lorenz C Blum, and Jean-Louis Reymond. Enumeration of 166 billion organic small molecules in the chemical universe database gdb-17. *Journal of chemical information and modeling*, 52(11):2864–2875, 2012.

S Saltsberger, I Steinberg, and Israel Gannot. Multilayer mie scattering model for investigation of intracellular structural changes in the nucleolus and cytoplasm. *International Journal of Optics*, 2012, 2012.

Bobak Shahriari, Kevin Swersky, Ziyu Wang, Ryan P Adams, and Nando De Freitas. Taking the human out of the loop: A review of bayesian optimization. *Proceedings of the IEEE*, 104(1):148–175, 2015.

Yichen Shen, Dexin Ye, Ivan Celanovic, Steven G Johnson, John D Joannopoulos, and Marin Soljačić. Optical broadband angular selectivity. *Science*, 343(6178):1499–1501, 2014.

Nino Shervashidze, Pascal Schweitzer, Erik Jan Van Leeuwen, Kurt Mehlhorn, and Karsten M Borgwardt. Weisfeiler-lehman graph kernels. *Journal of Machine Learning Research*, 12(9), 2011.

Yanpeng Shi, Xiaodong Wang, Wen Liu, Tianshu Yang, Rui Xu, and Fuhua Yang. Multilayer silver nanoparticles for light trapping in thin film solar cells, 2013.

Aditya Siddhant and Zachary C Lipton. Deep bayesian active learning for natural language processing: Results of a large-scale empirical study. *arXiv preprint arXiv:1808.05697*, 2018.

Martin Simonovsky and Nikos Komodakis. Dynamic edge-conditioned filters in convolutional neural networks on graphs. In *Proceedings of the IEEE conference on computer vision and pattern recognition*, pp. 3693–3702, 2017.

Jasper Snoek, Hugo Larochelle, and Ryan P Adams. Practical bayesian optimization of machine learning algorithms. *Advances in neural information processing systems*, 25:2951–2959, 2012.

Jasper Snoek, Oren Rippel, Kevin Swersky, Ryan Kiros, Nadathur Satish, Narayanan Sundaram, Mostofa Patwary, Mr Prabhat, and Ryan Adams. Scalable bayesian optimization using deep neural networks. In *International conference on machine learning*, pp. 2171–2180, 2015.

Jost Tobias Springenberg, Aaron Klein, Stefan Falkner, and Frank Hutter. Bayesian optimization with robust bayesian neural networks. *Advances in neural information processing systems*, 29:4134–4142, 2016.

Shengyang Sun, Guodong Zhang, Jiaxin Shi, and Roger Grosse. Functional variational bayesian neural networks. *arXiv preprint arXiv:1903.05779*, 2019.

Kevin Swersky, Jasper Snoek, and Ryan Prescott Adams. Freeze-thaw bayesian optimization. *arXiv preprint arXiv:1406.3896*, 2014.

Wenjie Tang and Graeme Henkelman. Charge redistribution in core-shell nanoparticles to promote oxygen reduction. *The Journal of chemical physics*, 130(19):194504, 2009.

The GPyOpt authors. GPyOpt: A bayesian optimization framework in python. `http://github.com/SheffieldML/GPyOpt`, 2016.

Sebastian Thrun. Lifelong learning algorithms. In *Learning to learn*, pp. 181–209. Springer, 1998.

Austin Tripp, Erik Daxberger, and José Miguel Hernández-Lobato. Sample-efficient optimization in the latent space of deep generative models via weighted retraining. *Advances in Neural Information Processing Systems*, 33, 2020.

Ryan Turner, David Eriksson, Michael J. McCourt, Juha Kiili, Eero Laaksonen, Zhen Xu, and Isabelle Guyon. Bayesian optimization is superior to random search for machine learning hyperparameter tuning: Analysis of the black-box optimization challenge 2020. In *NeurIPS*, 2020.

Tsuyoshi Ueno, Trevor David Rhone, Zhufeng Hou, Teruyasu Mizoguchi, and Koji Tsuda. Combo: an efficient bayesian optimization library for materials science. *Materials discovery*, 4:18–21, 2016.

Mark Van der Wilk, Carl Edward Rasmussen, and James Hensman. Convolutional gaussian processes. *arXiv preprint arXiv:1709.01894*, 2017.

Ian Walker and Ben Glocker. Graph convolutional gaussian processes. In *International Conference on Machine Learning*, pp. 6495–6504. PMLR, 2019.

Ke Wang, Geoff Pleiss, Jacob Gardner, Stephen Tyree, Kilian Q Weinberger, and Andrew Gordon Wilson. Exact gaussian processes on a million data points. *Advances in Neural Information Processing Systems*, 32, 2019.

Zi Wang, Clement Gehring, Pushmeet Kohli, and Stefanie Jegelka. Batched large-scale bayesian optimization in high-dimensional spaces. In *International Conference on Artificial Intelligence and Statistics*, pp. 745–754. PMLR, 2018.

Max Welling and Yee W Teh. Bayesian learning via stochastic gradient langevin dynamics. In *Proceedings of the 28th international conference on machine learning (ICML-11)*, pp. 681–688, 2011.

Yeming Wen, Dustin Tran, and Jimmy Ba. Batchensemble: an alternative approach to efficient ensemble and lifelong learning. *arXiv preprint arXiv:2002.06715*, 2020.

Florian Wenzel, Kevin Roth, Bastiaan S Veeling, Jakub Świątkowski, Linh Tran, Stephan Mandt, Jasper Snoek, Tim Salimans, Rodolphe Jenatton, and Sebastian Nowozin. How good is the bayes posterior in deep neural networks really? *arXiv preprint arXiv:2002.02405*, 2020.

Andrew Gordon Wilson, Zhiting Hu, Ruslan Salakhutdinov, and Eric P Xing. Deep kernel learning. In *Artificial intelligence and statistics*, pp. 370–378. PMLR, 2016.

James Wilson, Frank Hutter, and Marc Deisenroth. Maximizing acquisition functions for bayesian optimization. *Advances in Neural Information Processing Systems*, 31:9884–9895, 2018.

Eli Yablonovitch. Inhibited spontaneous emission in solid-state physics and electronics. *Physical review letters*, 58(20):2059, 1987.

Wanqian Yang, Lars Lorch, Moritz A Graule, Himabindu Lakkaraju, and Finale Doshi-Velez. Incorporating interpretable output constraints in bayesian neural networks. *arXiv preprint arXiv:2010.10969*, 2020.

Dongkun Zhang, Lu Lu, Ling Guo, and George Em Karniadakis. Quantifying total uncertainty in physics-informed neural networks for solving forward and inverse stochastic problems. *Journal of Computational Physics*, 397:108850, 2019a.

Ruqi Zhang, Chunyuan Li, Jianyi Zhang, Changyou Chen, and Andrew Gordon Wilson. Cyclical stochastic gradient mcmc for bayesian deep learning. *arXiv preprint arXiv:1902.03932*, 2019b.

A Appendix

A.1 Datasets

A.1.1 Nanoparticle Scattering

The multilayer nanoparticle consists of a lossless silica core surrounded by alternating spherical layers of lossless TiO_2 and lossless silica. The relative permittivity of silica is $\varepsilon_{\text{silica}} = 2.04$. The relative permittivity of TiO_2 is dispersive and depends on the wavelength of light:

$$\varepsilon_{\text{TiO}_2} = 5.913 + \frac{0.2441}{10^{-6}\lambda^2 - 0.0803} \tag{6}$$

where λ is the wavelength given in units of nm. The entire particle is surrounded by water, which has a relative permittivity of $\varepsilon_{\text{water}} = 1.77$.

For a given set of thicknesses, we analytically solve for the scattering spectrum, i.e. the scattering cross-section $\sigma(\lambda)$ as a function of wavelength λ, using Mie scattering as described in Qiu et al. (2012). The code for computing σ was adapted from Peurifoy et al. (2018).

The objective functions for the narrowband and highpass objectives are:

$$h_{\text{nb}}(\mathbf{z}) = \frac{\int_{\lambda\in\text{nb}} \sigma(\lambda)\, d\lambda}{\int_{\text{elsewhere}} \sigma(\lambda)\, d\lambda} \approx \frac{\sum_{i=126}^{145} z_i}{\sum_{i=1}^{125} z_i + \sum_{i=146}^{201} z_i} \tag{7}$$

$$h_{\text{hp}}(\mathbf{z}) = \frac{\int_{\lambda\in\text{hp}} \sigma(\lambda)\, d\lambda}{\int_{\text{elsewhere}} \sigma(\lambda)\, d\lambda} \approx \frac{\sum_{i=126}^{201} z_i}{\sum_{i=1}^{125} z_i}, \tag{8}$$

where $\mathbf{z} \in \mathbb{R}^{201}$ is the discretized scattering cross-section $\sigma(\lambda)$ from $\lambda = 350\,\text{nm}$ to $750\,\text{nm}$.

A.1.2 Photonic Crystal

The photonic crystal (PC) consists of periodic unit cells with periodicity $a = 1\,\text{au}$, where each unit cell is depicted as a "two-tone" image, with the white regions representing silicon with permittivity $\varepsilon_1 = 11.4$ and black regions representing vacuum (or air) with permittivity $\varepsilon_0 = 1$.

The photonic crystal (PC) structure is defined by a spatially varying permittivity $\varepsilon(x, y) \in \{\varepsilon_0, \varepsilon_1\}$ over a 2D periodic unit cell with spatial coordinates $x, y \in [0, a]$. To parameterize ε, we choose a level set of a Fourier sum function ϕ, defined as a linear combination of plane waves with frequencies evenly spaced in the reciprocal lattice space up to a maximum cutoff. Intuitively, the upper limit on the frequencies roughly corresponds to a lower limit on the feature size such that the photonic crystal remains within reasonable fabrication constraints. Here we set the cutoff such that there are 25 complex frequencies corresponding to 50 real coefficients $\mathbf{c} = (c_1, c_2, ..., c_{50})$.

Explicitly, we have

$$\phi[\mathbf{c}](x, y) = \Re\left\{\sum_{k=1}^{25} (c_k + ic_{k+25})\, e^{2\pi i(n_x x + n_y y)/a}\right\}, \tag{9}$$

where each exponential term is composed from the 25 different pairs $\{n_x, n_y\}$ with $n_x, n_y \in \{-2, -1, 0, 1, 2\}$. We then choose a level-set offset Δ to determine the PC structure, where regions with $\phi > \Delta$ are assigned to be silicon and regions where $\phi \leq \Delta$ are vacuum. Thus, the photonic crystal unit cell topology is parameterized by a 51-dimensional vector, $[c_1, c_2, ..., c_{50}, \Delta] \in \mathbb{R}^{51}$. More specifically,

$$\varepsilon(x, y) = \varepsilon[\mathbf{c}, \Delta](x, y) = \begin{cases} \varepsilon_1 & \phi[\mathbf{c}](x, y) > \Delta \\ \varepsilon_0 & \phi[\mathbf{c}](x, y) \leq \Delta \end{cases}, \tag{10}$$

which is discretized to result in a 32×32 pixel image $\mathbf{v} \in \{\varepsilon_0, \varepsilon_1\}^{32\times 32}$. This formulation also has the advantage of enforcing periodic boundary conditions.

For each unit cell, we use the MIT Photonics Bands (MPB) software (Johnson & Joannopoulos, 2001) to compute the band structure of the photonic crystal, $\omega(\mathbf{k})$, up to the lowest 10 bands, using a 32×32 spatial resolution (or equivalently, 32×32 k-points over the Brillouin zone $-\frac{\pi}{a} < k < \frac{\pi}{a}$). We also extract the group velocities at each k-point and compute the density-of-states (DOS) via an extrapolative technique, adapted from Liu et al. (2018). The DOS is computed at a resolution of 20,000 points, and a Gaussian filter of kernel size 100 is used to smooth the DOS spectrum. To normalize the frequency scale across the different unit cells, the frequency is rescaled via $\omega\sqrt{\varepsilon_{avg}} \to \omega_{norm}$, where $\varepsilon_{avg} = \frac{1}{a^2}\int_0^a \int_0^a \varepsilon(x,y)\,dx\,dy \approx \frac{1}{(32)^2}\sum_{i,j} v_{i,j}$ is the average permittivity over all pixels. Finally, the DOS spectrum is truncated at $\omega_{norm} = 1.2$ and interpolated using 500 points to give $\mathbf{z} \in \mathbb{R}^{500}$.

The objective function aims to minimize the DOS in a small frequency range and maximize it elsewhere. We use the following:

$$h_{\text{DOS}}(\mathbf{z}) = \frac{\sum_{i=1}^{300} z_i + \sum_{i=351}^{500} z_i}{1 + \sum_{i=301}^{350} z_i}, \tag{11}$$

where the 1 is added in the denominator to avoid singular values.

A.1.3 Organic Molecule Quantum Chemistry

The Smooth Overlap of Atomic Positions (SOAP) descriptor (De et al., 2016) uses smoothed atomic densities to describe local environments for each atom in the molecule through a fixed-length feature vector, which can then be averaged over all the atoms in the molecule to produce a fixed-length feature vector for the molecule. This descriptor is invariant to translations, rotations, and permutations. We use the SOAP descriptor implemented by DScribe (Himanen et al., 2020) using the recommended parameters: local cutoff `rcut` $= 5$, number of radial basis functions `nmax` $= 8$, and maximum degree of spherical harmonics `lmax` $= 8$. We use `outer` averaging, which averages over the power spectrum of different sites.

The graph representation of each molecule is processed by the Spektral package (Grattarola & Alippi, 2020). Each graph is represented by a node feature matrix $\mathbf{X} \in \mathbb{R}^{s \times d_n}$, an adjacency matrix $\mathbf{A} \in \mathbb{R}^{s \times s}$, and an edge matrix $\mathbf{E} \in \mathbb{R}^{e \times d_e}$, where s is the number of atoms in the molecule, e is the number of bonds, and d_n, d_e are the number of features for nodes and edges, respectively.

The properties that we use from the QM9 dataset are listed in Table 1. We separate these properties into two categories: (1) the *ground state quantities* which are calculated from a single DFT calculation of the molecule and include geometric, energetic, and electronic quantities, and (2) the *thermodynamic quantities* which are typically calculated from a molecular dynamics simulation.

The auxiliary information for this task consist of the properties listed in Table 1 that are in the same category as the objective property, as these properties would be calculated together. The objective function then simply picks out the corresponding feature from the auxiliary information. More precisely, for the ground state objectives, the auxiliary information is

$$\mathbf{z} = \left[A, B, C, \mu, \alpha, \epsilon_{\text{HOMO}}, \epsilon_{\text{LUMO}}, \epsilon_{\text{gap}}, \langle R^2 \rangle\right] \in \mathbb{R}^9,$$

and the objective functions are

$$h_\alpha(\mathbf{z}) = z_5$$
$$h_{\alpha - \epsilon_{\text{gap}}}(\mathbf{z}) = \frac{z_5 - 6}{191} - \frac{z_8 - 0.02}{0.6}$$

where the quantities for the latter objective are normalized so that they have the same magnitude.

A.2 Bayesian Optimization

Our algorithm for Bayesian optimization using auxiliary information $\mathbf{z}$ is shown in Algorithm 1. This algorithm reduces to the basic BO algorithm in the case where h is the identity function and $\mathcal{Z} = \mathcal{Y}$ such that we can ignore mention of $\mathbf{z}$ in Algorithm 1.

Table 1: List of properties from the QM9 dataset used as labels

Property	Unit	Description
Ground State Quantities		
A	GHz	Rotational constant
B	GHz	Rotational constant
C	GHz	Rotational constant
μ	D	Dipole moment
α	a_0^3	Isotropic polarizability
ϵ_{HOMO}	Ha	Energy of HOMO
ϵ_{LUMO}	Ha	Energy of LUMO
ϵ_{GAP}	Ha	Gap ($\epsilon_{\text{LUMO}} - \epsilon_{\text{HOMO}}$)
$\langle R^2 \rangle$	a_0^2	Electronic spatial extent
Thermodynamic Quantities at 298.15 K		
U	Ha	Internal energy
H	Ha	Enthalpy
G	Ha	Free energy
C_V	$\frac{\text{cal}}{\text{mol K}}$	Heat capacity

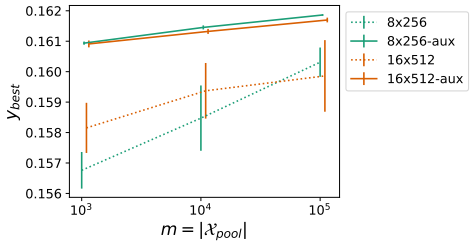

Figure 6: Effect of $m = |\mathcal{X}_{\text{pool}}|$ used in the inner optimization loop to maximize the acquisition function on overall BO performance. y_{best} is taken from the narrowband objective function using the ensemble architecture. The "aux" in the legend denotes using auxiliary information and the numbers represent the architecture (i.e. 8 layers of 256 units or 16 layers of 512 units).

Algorithm 1 Bayesian optimization with auxiliary information

1: **Input:** Labelled dataset $\mathcal{D}_{\text{train}} = \{(\mathbf{x}_n, \mathbf{z}_n, y_n)\}_{n=1}^{N_{\text{start}}=5}$
2: **for** $N = 5$ **to** 1000 **do**
3: Train $\mathcal{M}\colon \mathcal{X} \to \mathcal{Z}$ on $\mathcal{D}_{\text{train}}$
4: Form an unlabelled dataset, $\mathcal{X}_{\text{pool}}$
5: Find $\mathbf{x}_{N+1} = \arg\max_{\mathbf{x}\in\mathcal{X}_{\text{pool}}} \alpha\left(\mathbf{x}; \mathcal{M}, \mathcal{D}_{\text{train}}\right)$
6: Label the data $\mathbf{z}_{N+1} = g(\mathbf{x}_{N+1})$, $y_{N+1} = h(\mathbf{z}_{N+1})$
7: $\mathcal{D}_{\text{train}} = \mathcal{D}_{\text{train}} \cup \left(\mathbf{x}_{N+1}, \mathbf{z}_{N+1}, y_{N+1}\right)$
8: **end for**

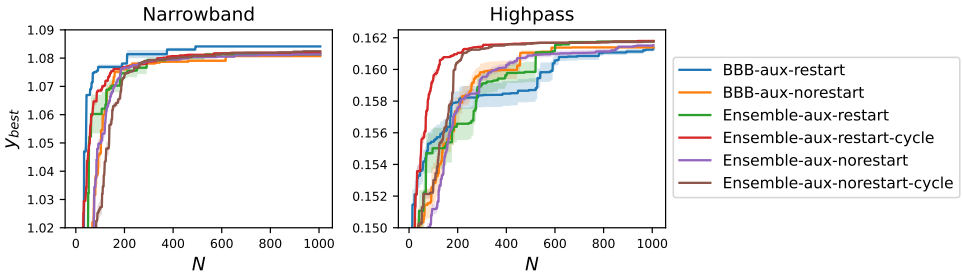

Figure 7: Effect of restarting the BNN training from scratch in each BO iteration.

As mentioned in the main text, the inner optimization loop in line 5 of Algorithm 1 is performed by finding the maximum value of α over a pool of $|\mathcal{X}_{\text{pool}}|$ randomly sampled points. We can see in Figure 6 that increasing $|\mathcal{X}_{\text{pool}}|$ in the acquisition step tends to improve BO performance. Thus, there is likely further room for improvement of the inner optimization loop using more sophisticated algorithms, possibly using the gradient information provided by BNNs.

A.3 Continued Training

As mentioned in Section 2.2 of the main text, the BNN is ideally trained from scratch until convergence in each iteration loop, although this comes at a great computational cost. An alternative is the warm restart method of continuing the training from the previous iteration which enables the model's training loss to converge in only a few epochs. However, as shown in Figure 7, we have found that naive continued training can result in poor BO performance. This is likely because training does not converge for the new data point $\mathcal{D}_{\text{new}} = (\mathbf{x}_{N+1}, y_{N+1})$ relative to the rest of the data under a limited computational budget, resulting in the acquisition function possibly labeling similar points in consecutive iterations. To mitigate this, we use the cosine annealing learning rate proposed in Loshchilov & Hutter (2016). This also has the advantage of allowing the model to more easily explore a multimodal posterior (Huang et al., 2017). Note that this is similar to "continual learning," which is an open and active sub-problem in machine learning research (Thrun, 1998; Parisi et al., 2019)

A.4 Models and Hyperparameters

Unless otherwise stated, we set $N_{\text{MC}} = 30$ and choose the next data point to label by maximizing EI on a pool of $|\mathcal{X}_{\text{pool}}| = 10^5$ randomly sampled points.

All BNNs other than the infinitely-wide networks are implemented in TensorFlow v1. Models are trained using the Adam optimizer using the cosine annealing learning rate with a base learning rate of 10^{-3} (Loshchilov & Hutter, 2016). All hidden layers use ReLU as the activation function, and no activation function is applied to the output layer.

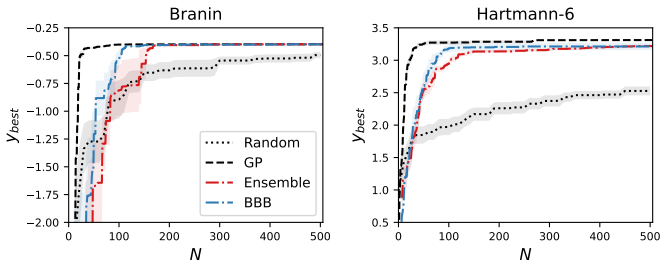

Figure 8: BO results for the Branin and Hartmann-6 functions.

Infinite-width neural networks are implemented using the Neural Tangents library (Novak et al., 2020). We use two different types of infinite networks: (1) "GP-" refers to a closed form expression for Gaussian process inference using the neural network as a kernel, and (2) "INF-" refers to an infinite ensemble of infinite-width networks that have been "trained" with continuous gradient descent for an infinite time. We compare NNGP and NTK kernels as well as the parameterization of the layers. By default, we use the NTK parameterization, but we also use the standard parameterization, denoted by "-STD".

We implement BO using GPs with a Matérn kernel using the GPyOpt library (The GPyOpt authors, 2016). The library optimizes over the acquisition function in the inner loop using the L-BFGS algorithm.

LIPO (Malherbe & Vayatis, 2017) is implemented in the dlib library (King, 2009). DIRECT-L (Gablonsky & Kelley, 2001) is implemented in the NLopt library (Johnson, 2010). CMA-ES is implemented in the pycma library (Hansen et al., 2019).

Additional Results

A.5 Test Functions

We test BO on several common synthetic functions used for optimization, namely the Branin and 6-dimensional Hartmann functions. We use BNNs with 4 hidden layers and 256 units in each hidden layer, where each hidden layer is followed by a ReLU activation function. Plots of the best value y_{best} at each BO iteration are shown in Figure 8. As expected, GPs perform the best. Ensembles and BBB also perform competitively and much better than random sampling, showing that deep BO is viable even for low-dimensional black-box functions.

A.6 Nanoparticle Scattering

Detailed BO results for the nanoparticle scattering problem are shown in Table 2.

All the BNNs used for the nanoparticle scattering problem use an architecture consisting of 8 hidden layers with 256 units each, with the exception of BOHAMIANN where we used the original architecture consisting of 2 hidden layers with 50 units each. The infinite-width neural networks for the nanoparticle task consist of 8 hidden layers of infinite width, each of which are followed by ReLU activation functions.

We also experiment with KL annealing in BBB, a proposed method to improve the performance of variational methods for BNNs in which the weight of the KL term in the loss function is slowly increased throughout training Wenzel et al. (2020). For these experiments, we exponentially anneal the KL term with weight $\sigma_{KL}(i) = 10^{i/500-5}$ as a function of epoch i when training from scratch; during the continued training, the weight is held constant at $\sigma_{KL} = 10^{-3}$.

KL annealing in the BBB architecture significantly improves performance for the narrowband objective, although results are mixed for the highpass objective. Additionally, KL annealing has the downside of introducing more parameters that must be carefully tuned for optimal performance. MNF performs poorly, especially on the highpass objective where it is comparable to random sampling, and we have found that

Table 2: BO results for the nanoparticle scattering problem. * denotes that y_{best} is measured at $N = 100$ due to computational constraints

Model	Narrowband				Highpass			
	y_{best} at $N = 250$		y_{best} at $N = 1000$		y_{best} at $N = 250$		y_{best} at $N = 100$	
	Mean	SE	Mean	SE	Mean	SE	Mean	SE
GP	0.1606	0.0005	0.1621	0.0001	1.0839	0.0017	1.0851	0.0008
GP-aux	*0.1541	0.0019	-	-	*1.0110	0.0234	-	-
Ensemble	0.1558	0.0011	0.1607	0.0003	1.0729	0.0025	1.077	0.0021
Ensemble-aux	0.1578	0.0014	0.1593	0.0013	1.0783	0.0003	1.0822	0.001
BBB	0.1596	0.0006	0.1596	0.0006	1.0753	0.0005	1.0753	0.0005
BBB-aux	0.1601	0.001	0.1601	0.001	1.076	0.0028	1.076	0.0028
BBB-Anneal	0.1598	0.001	0.1611	0.0001	1.0813	0.0003	1.0821	0.0005
BBB-aux-Anneal	0.1613	0.0003	0.1619	0	1.0826	0.0008	1.0834	0.0005
MNF	0.15	0.0005	0.1547	0.0004	1.027	0.005	1.0312	0.0036
MNF-aux	0.1549	0.0014	0.1569	0.0006	0.9957	0.0168	1.028	0.0157
Neural Linear	0.1543	0.002	0.1579	0.0015	1.0798	0.0007	1.0836	0.0007
BOHAMIANN	0.1616	0.0001	-	-	1.0717	0.0031	-	-
Inf-NNGP	0.1541	0.0011	0.157	0.0009	1.055	0.0036	1.0653	0.0022
Inf-NTK	0.1536	0.0008	0.1571	0.001	1.041	0.004	1.0612	0.0011
Inf-NNGP-std	0.1551	0.0006	0.1598	0.0006	1.0615	0.0043	1.069	0.0018
Inf-NTK-std	0.1564	0.0006	0.1607	0.0001	1.0607	0.0039	1.0761	0.0014
GP-NNGP	0.1582	0.0007	0.1609	0.0001	1.0621	0.0027	1.0694	0.0019
GP-NTK	0.1573	0.001	0.1611	0.0001	1.0667	0.0032	1.0732	0.0012
GP-NNGP-std	0.1562	0.0008	0.1595	0.001	1.0615	0.0058	1.0718	0.0024
GP-NTK-std	0.1592	0.0011	0.1608	0.0002	1.0641	0.0033	1.0704	0.0017
Random	0.1527	0.0008	0.1555	0.0006	1.0053	0.0063	1.0362	0.0047
LIPO	0.1604	0.0016	0.1619	0.0006	1.0792	0.0066	1.087	0.0034
DIRECT-L	0.1544	0	0.156	0	1.0777	0	1.0801	0
CMA	0.1424	0.0046	0.143	0.0048	1.059	0.0117	1.076	0.0127

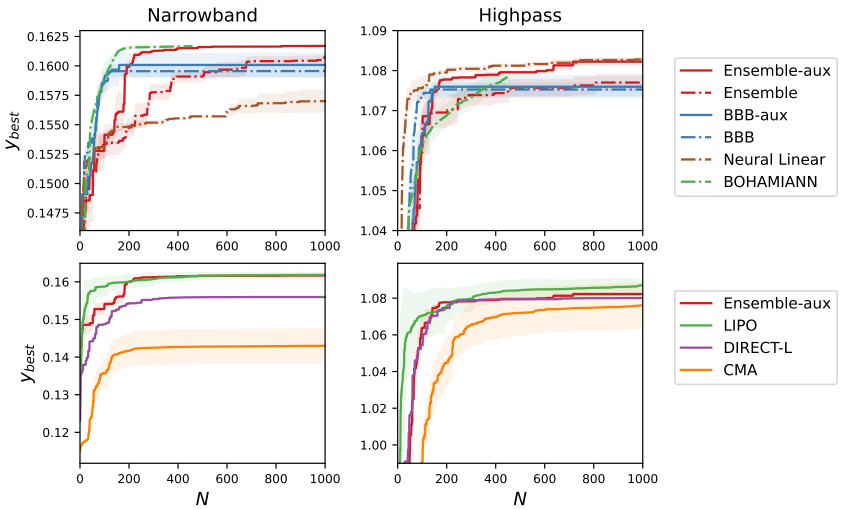

Figure 9: Additional optimization result curves for the nanoparticle scattering task. (Top) Various BNNs. Note that results using auxiliary information are denoted by a solid line, while those that do not are denoted by a dashed line. Also note that the y-axis is zoomed in to differentiate the curves. (Bottom) Various non-BO algorithms. Ensemble-aux is replicated here for ease of comparison.

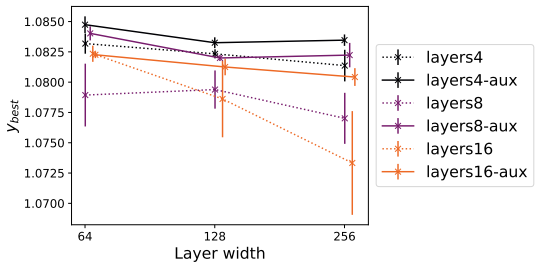

Figure 10: Comparison of y_{best} at $N = 1000$ for the nanoparticle narrowband objective function for a variety of neural network sizes. All results are ensembles, and "aux" denotes using auxiliary information.

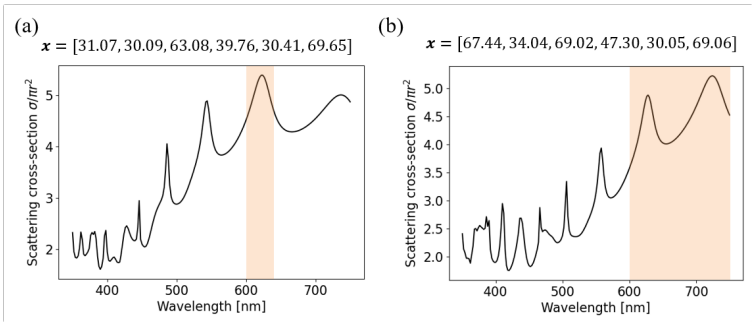

Figure 11: Examples of optimized nanoparticles and their scattering spectrum using the "Ensemble-aux" architecture for the (a) narrowband and (c) highpass objectives. Orange shaded regions mark the range over which we wish to maximize the scattering.

MNF is quite sensitive to the choice of hyperparameters for uncertainty estimates even on simple regression problems.

The different variants infinite-width neural networks do not perform as well as the BNNs on both objective functions, despite the hyper-parameter search.

LIPO seems to perform as well as GPs on both objective functions, which is impressive given the computational speed of the LIPO algorithm. Interestingly DIRECT-L does not perform as well as LIPO or GPs on the narrowband objective, and actually performs comparably to random sampling on the highpass objective. Additionally, CMA performs poorly on both objectives, likely due to the highly multimodal nature of the objective function landscape.

We also look at the effect of model size in terms of number of layers and units in Figure 10 for ensembles. While including auxiliary information clearly improves performance across all architectures, there is not a clear trend of performance with respect to the model size. Thus, the performance of BO seems to be somewhat robust to the exact architecture as long as the model is large enough to accurately and efficiently train on the data.

Examples of the optimized structures by the "Ensemble-aux" architecture are shown in Figure 11. We can see that the scattering spectra peak in the shaded region of interest, as desired by the respective objective functions.

A.7 Photonic Crystal

The BNN and BCNN architectures that we use for the PC task are listed in Table 3. The size of the "FC" architectures are chosen to have a similar number of parameters as their convolutional counterparts. Unless otherwise stated, all results in the main text and here use the "Conv-TI" and "FC" architectures for BCNNs and BNNs, respectively.

Table 3: Various architectures for BNNs and BCNNs used in the PC problem. Numbers represent the number of channels and units for the convolutional and fully-connected layers, respectively. All convolutional layers use 3×3-sized filters with stride $(1, 1)$ and periodic boundaries. "MP" denotes max-pooling layers of size 2×2 with stride $(2, 2)$, and "AP" denotes average-pooling layers of size 2×2 with stride $(1, 1)$. "Conv" denotes BCNNs whereas "FC" denotes BNNs (containing only fully-connected layers) that act on the level-set parameterization $\mathbf{x}$ rather than on the image $\mathbf{v}$. "TI" denotes translation invariant architectures, whereas "TD" denotes translation dependent architectures (i.e. not translation invariant).

Architecture	Convolutional Layers	Fully-connected Layers
Conv-TI	16-MP-32-MP-64-MP-128-MP-256	256-256-256-256
Conv-TD	8-AP-8-MP-16-AP-32-MP-32-AP	256-256-256-256
FC	n/a	256-256-256-256-256

Table 4: Select BO results for the PC problem. * denotes that y_{best} is measured at $N = 130$ due to computational constraints. † denotes that y_{best} is measured at $N = 750$ due to computational constraints.

Model	PC-A				PC-B			
	y_{best} at $N = 250$		y_{best} at $N = 1000$		y_{best} at $N = 250$		y_{best} at $N = 100$	
	Mean	SE	Mean	SE	Mean	SE	Mean	SE
GP	548	450	2109	448	781	394	3502	49
GP-aux	*16	4	-	-	*9	1	-	-
Ensemble	30	2	841	448	216	145	1318	465
Ensemble-aux	305	217	1310	509	2909	408	3633	130
ConvEnsemble	1140	471	2375	371	390	263	2070	505
ConvEnsemble-aux	2623	558	3468	120	3752	106	4002	92
BBB	75	31	350	207	704	502	780	485
BBB-aux	39	7	413	313	554	371	1605	544
ConvBBB	712	416	1486	490	928	600	930	599
ConvBBB-aux	2109	583	3124	43	1761	724	1928	711
NeuralLinear	1009	549	1235	481	685	488	2853	291
ConvNeuralLinear	1160	540	2524	479	1643	596	2722	647
Conv-Inf-NNGP	29	8	322	181	21	7	157	42
Conv-Inf-NTK	49	32	425	322	28	7	907	711
Conv-GP-NNGP	15	2	221	118	37	5	830	533
Conv-GP-NTK	20	10	194	139	34	12	85	45
Conv-Inf-NNGP-std	17	3	732	432	66	15	889	442
Conv-Inf-NTK-std	52	31	99	64	8	0	27	12
Conv-GP-NNGP-std	20	7	†101	59	100	55	†124	49
Conv-GP-NTK-std	13	5	†132	77	7	0	†686	575
Random	141	61	402	184	471	398	485	395
LIPO	940	1073	1280	1073	1837	1792	2266	1626
DIRECT-L	20	0	4351	1	8	0	2525	38
CMA	9	1	4078	126	10	3	1777	969

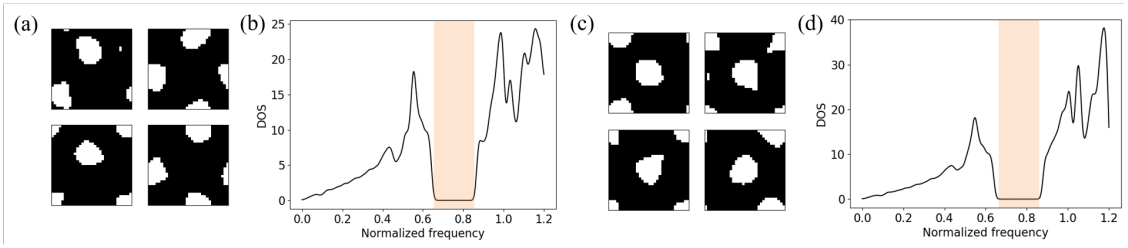

Figure 12: Examples of optimized photonic crystal unit cells over multiple trials for (a) PC-A distribution and (c) PC-B distribution. (b,d) Examples of the optimized DOS. Note that the DOS has been minimized to nearly zero in a thin frequency range. Orange shaded regions mark the frequency range in which we wish to minimize the DOS. All results were optimized by the "Ensemble-aux" architecture.

The infinite-width convolutional neural networks (which act as convolutional kernels for GPs) in the PC task consist of 5 convolutional layers followed by 4 fully-connected layers of infinite width. Because the pooling layers in the Neural Tangents library are currently too slow for use in application, we increased the size of the filters to 5×5 to increase the receptive field of each filter.

Detailed BO results for the PC problem are shown in Table 4. For algorithms that optimize over the level set parameterization $\mathbb{R}^{51}$, we see that GPs perform consistently well, although BNNs using auxiliary information (e.g. Ensemble-Aux) can outperform GPs. DIRECT-L and CMA perform extremely well on the PC-A distribution but performs worse than GP on the PC-B distribution.

Adding convolutional layers and auxiliary information improves performance such that BCNNs significantly outperform GPs. Interestingly, the infinite-width networks perform extremely poorly, although this may be due to a lack of pooling layers in their architecture which limits the receptive field of the convolutions.

Examples of the optimized structures by the "Ensemble-aux" architecture are shown in Figure 12. The photonic crystal unit cells generally converged to the same shape: a square lattice of silicon posts with periodicity $\sqrt{2}a$.

A.8 Organic Molecule Quantum Chemistry

The Bayesian graph neural networks (BGNNs) used for the chemical property optimization task consist of 4 edge-conditioned graph convolutional layers with 32 channels each, followed by a global average pooling operation, followed by 4 fully-connected hidden layers of 64 units each. The edge-conditioned graph convolutional layers Simonovsky & Komodakis (2017) are implemented by Spektral Grattarola & Alippi (2020).

More detailed results for the quantum chemistry dataset are shown in Table 5 and Figure 13. The architecture with the Bayes by Backprop variational approximation applied to every layer including the graph convolutional layers ("BBB"), performs extremely poorly, even worse than random sampling in some cases. However, only making the fully-connected layers Bayesian ("BBB-FC") performs surprisingly well.

Ensembles trained with auxiliary information ("Ensemble-aux") and neural linear ("NeuralLinear") perform the best on all objective functions. Adding auxiliary information to ensembles helps for the α objective function, and neither helps nor hurts for the other objective functions. Additionally, BNNs perform at least as well or significantly better than GPs in all cases. GPs perform comparably or worse than random sampling in several cases.

"VAE-GP" uses a modified version of the latent-space optimization method implementation provided by Tripp et al. (2020). Rather than optimizing over a continuous latent space of the VAE, we feed the data pool through the VAE encoder to find their latent space representation, and then apply the acquisition function to the latent points to pick out the best unlabeled point to sample. We keep as many hyperparameters the same as the original implementation as possible, with the exception of the weighted retraining which we forgo since we have a fixed data pool that was used to train the VAE. This setup is similar to "GraphNeuralLinear" in that a deep learning architecture is used to encode the molecule as a vector,

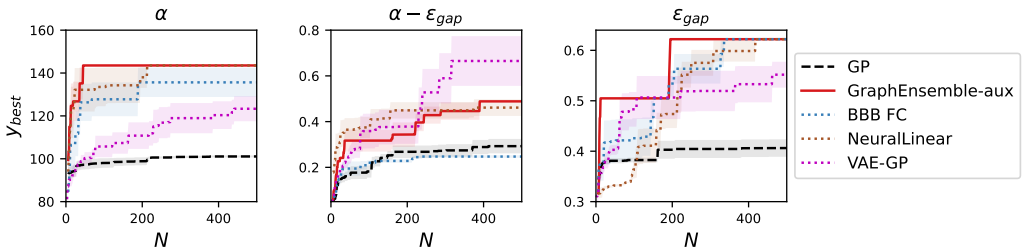

Figure 13: Additional BO results for several different objective functions on the chemistry dataset. GP and GraphEnsemble-aux curves are replicated from the main text for convenience.

Table 5: BO results for the four different quantum chemistry objective functions. * denotes that y_{best} is measured at $N = 100$ due to computational constraints.

Model	y_{best} at $N = 500$							
	ϵ_{gap}		$-\epsilon_{\text{gap}}$		α		$\alpha - \epsilon_{\text{gap}}$	
	Mean	SD	Mean	SD	Mean	SD	Mean	SD
GP	0.41	0.04	−0.10	0.02	101.08	1.05	0.29	0.07
GraphGP	*0 62	0.00	* − 0.10	0.02	*131.99	14.59	*0.24	0.03
GraphEnsemble	0.62	0.00	−0.10	0.00	143.53	0.00	0.49	0.00
GraphEnsemble-aux	0.62	0.00	−0.10	0.00	143.53	0.00	0.49	0.00
GraphBBB	0.38	0.01	−0.11	0.01	94.46	1.16	-	-
GraphBBB-FC	0.62	0.00	−0.10	0.00	135.64	13.67	0.25	0.01
GraphNeuralLinear	0.62	0.00	−0.09	0.01	143.53	0.00	0.46	0.09
VAE-GP	0.62	0.06	-	-	123.33	13.02	0.61	0.34
Random	0.38	0.02	−0.11	0.03	105.19	7.87	0.29	0.07

although "GraphNeuralLinear" is retrained in each iteration. The results for this experiment show that "VAE-GP" performs worse than BNNs on two of the four objective functions and better on one objective.

A.9 Compute

All experiments were carried out on systems with NVIDIA Volta V100 GPUs and Intel Xeon Gold 6248 CPUs. All training and inference using neural network-based models, graph kernels, and infinite-width or infinite-ensemble approximations are carried out on the GPUs. All other models are carried out on the CPUs.